electronics

MDPI

Communication

Investigation of the Effect of Different SiN_x Thicknesses on the Characteristics of AlGaN/GaN High-Electron-Mobility Transistors in Ka-Band

Che-Wei Hsu [1], Yueh-Chin Lin [1], Ming-Wen Lee [2] and Edward-Yi Chang [1,2,*]

[1] Department of Materials Science and Engineering, National Yang Ming Chiao Tung University, Hsinchu City 30010, Taiwan; tonyhsu.c@nycu.edu.tw (C.-W.H.)

[2] International College of Semiconductor Technology, National Yang Ming Chiao Tung University, Hsinchu City 30010, Taiwan; ericlmw.st06@nycu.edu.tw

* Correspondence: edc@nycu.edu.tw

Abstract: The effect of different SiN_x thicknesses on the performance of AlGaN/GaN high-electron-mobility transistors (HEMTs) was investigated in this paper. The current, transconductance (G_m), cut-off frequency (f_T), maximum oscillation frequency (f_{max}), power performance, and output third-order intercept point (OIP3) of devices with three different SiN_x thicknesses (150 nm, 200 nm, and 250 nm) were measured and analyzed. The DC measurements revealed an increase in both the drain-source current (I_{DS}) and G_m values of the device with increasing SiN_x thickness. The S-parameter measurement results show that devices with a higher SiN_x thickness exhibit improved f_T and f_{max}. Regarding power performance, thicker SiN_x devices also improve the output power density (P_{out}) and power-added efficiency (PAE) in the Ka-band. In addition, the two-tone measurement results at 28 GHz show that the OIP3 increased from 35.60 dBm to 40.87 dBm as the SiN_x thickness increased from 150 nm to 250 nm. The device's characteristics improved by appropriately increasing the SiN_x thickness.

Keywords: AlGaN/GaN HEMTs; SiN_x thickness; gate stem height; output third-order intercept point; Ka-band; linearity

check for updates

Citation: Hsu, C.-W.; Lin, Y.-C.; Lee, M.-W.; Chang, E.-Y. Investigation of the Effect of Different SiN_x Thicknesses on the Characteristics of AlGaN/GaN High-Electron-Mobility Transistors in Ka-Band. *Electronics* **2023**, *12*, 4336. https://doi.org/10.3390/electronics12204336

Academic Editor: Koon Hoo Teo

Received: 3 October 2023
Revised: 15 October 2023
Accepted: 17 October 2023
Published: 19 October 2023

1. Introduction

Recently, extensive research has been conducted on the application of AlGaN/GaN high-electron-mobility transistors (HEMTs) in high-frequency microwave power devices, ranging from essential everyday needs to defense applications such as 5G small-cell base stations, satellite communications, defense and military applications, and industrial radar [1–6]. Compared to other III-V compound semiconductors, GaN materials possess excellent characteristics, such as a wide bandgap, high electron mobility, high saturation velocity, and a high breakdown field [7–9]. Additionally, the combination of GaN and AlGaN layers forms a two-dimensional electron gas (2DEG) at the interface, which is characterized by a high electron concentration. These excellent characteristics allow GaN devices to maintain high output power at higher frequencies [10–12].

In the face of the arrival and commercialization of the fifth generation of mobile communication (5G), characterized by faster transmission speeds, low latency, large bandwidth, and high density, it is advantageous for the development of services such as big data, the Internet of Things (IoT), and Artificial Intelligence (AI) [13,14]. These advancements can drive high-quality audiovisual entertainment, self-driving cars, drones, smart healthcare, intelligent factories, smart retail, smart cities, and other value-added innovative applications. This has become a focal point of development in countries around the world. Due to the growing demand for high-speed transmission in 5G communication, there is an increasing need for high-frequency devices operating in the Ka-band to support wider bandwidth requirements [15–18].

In wireless communication, when two or more signals pass through nonlinear amplifier devices, intermodulation distortion (IMD) occurs. Because IMD generates unwanted spurious emissions, it leads to an increase in the occupied bandwidth and interferes with adjacent channels, ultimately reducing audio clarity or increasing spectral occupancy. Among the nonlinear distortions generated by devices within the system, the third-order intermodulation distortion (IM3) is the most influential factor [19–21]. It is closest to the main signal, difficult to filter out, and easily affects the signal quality. Therefore, improving device linearity by enhancing the performance metrics, including the output third-order intercept point (OIP3) and reducing IM3, is an important concern. The literature has put forward various methods to enhance HEMT linearity, including δ-Doped [22], gate dielectric [23], N-Polar GaN MIS-HEMT [24], selective-area charge implantation [25], fin-like configuration [26], and etched-fin gate structure [27]. For traditional AlGaN/GaN HEMTs, the transconductance (G_m) of the device rapidly decreases after reaching its peak as the gate-source voltage (V_{GS}) increases, resulting in severe nonlinearity [28]. To improve the DC characteristics of a device, many studies have proposed methods such as modifying the device structure or reducing the gate leakage current to enhance the overall DC and RF performance of the device [29–32]. However, there is limited literature on improving device performance by increasing the SiN_x thickness [33].

In this study, we investigate the effect of different SiN_x thicknesses on the characteristics of AlGaN/GaN HEMT devices in the Ka-band. The DC characteristics, S-parameter measurement, power performance, and OIP3 of devices with three different SiN_x thicknesses (150 nm, 200 nm, and 250 nm) were measured. The measurement results demonstrate an enhancement in the device's performance as the SiN_x thickness increases to 250 nm.

2. Materials and Methods

The AlGaN/GaN HEMT heterostructure used in this study was grown on a 4-inch SiC substrate using metal–organic chemical vapor deposition (MOCVD). A cross-sectional schematic diagram of the AlGaN/GaN HEMT is displayed in Figure 1. The dimensions of the device were as follows: L_g is 150 nm, H_{head} is 350 nm, and the thicknesses of the SiN_x layer (t_{SiNx}) were 150 nm, 200 nm, or 250 nm. The device fabrication process flow is shown in Figure 2. Device fabrication began with the Ohmic contact formation of Ti/Al/Ni/Au. The Ohmic metal layers were deposited using an E-gun evaporator, followed by rapid thermal annealing (RTA) at 830 °C for 30 s in a nitrogen atmosphere to form Ohmic contacts. Next, device isolation was achieved using boron ion implantation. A photoresist was used as a mask to protect the active region, and boron ions (B^{11+}) were implanted using an ion implantation machine to complete the device isolation process. To define the gate region, the first SiN_x passivation layer was deposited using plasma-enhanced chemical vapor deposition (PECVD). The thicknesses of the first SiN_x layers (t_{SiNx}) were 150 nm, 200 nm, and 250 nm. Afterward, stepper lithography was performed twice to complete the gate fabrication. The first step of stepper lithography defined the areas for etching the first SiN_x film, followed by etching using inductively coupled plasma (ICP). The second step of stepper lithography defined the areas for depositing the gate metal. After two steps of stepper lithography, the Ni/Au gate metal stack was deposited using an E-gun evaporator to complete the gate fabrication. Before depositing the gate metal, the wafer was immersed in a diluted HCl solution for one minute to remove any natural oxides from the AlGaN barrier layer. After gate fabrication was completed, the first SiN_x layer was removed using ICP, followed by the deposition of the second SiN_x layer using PECVD. Finally, for metallization, holes were opened in the passivation film via ICP, and then a 1.5 μm thickness of Au metallization layer was deposited.

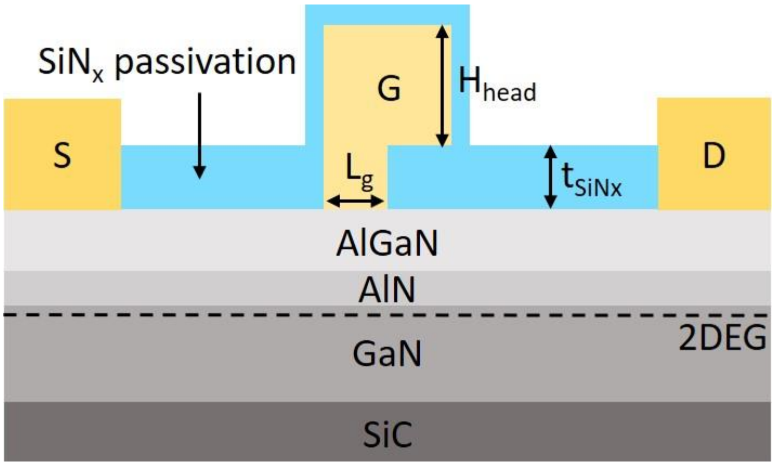

Figure 1. Schematic of the AlGaN/GaN HEMT.

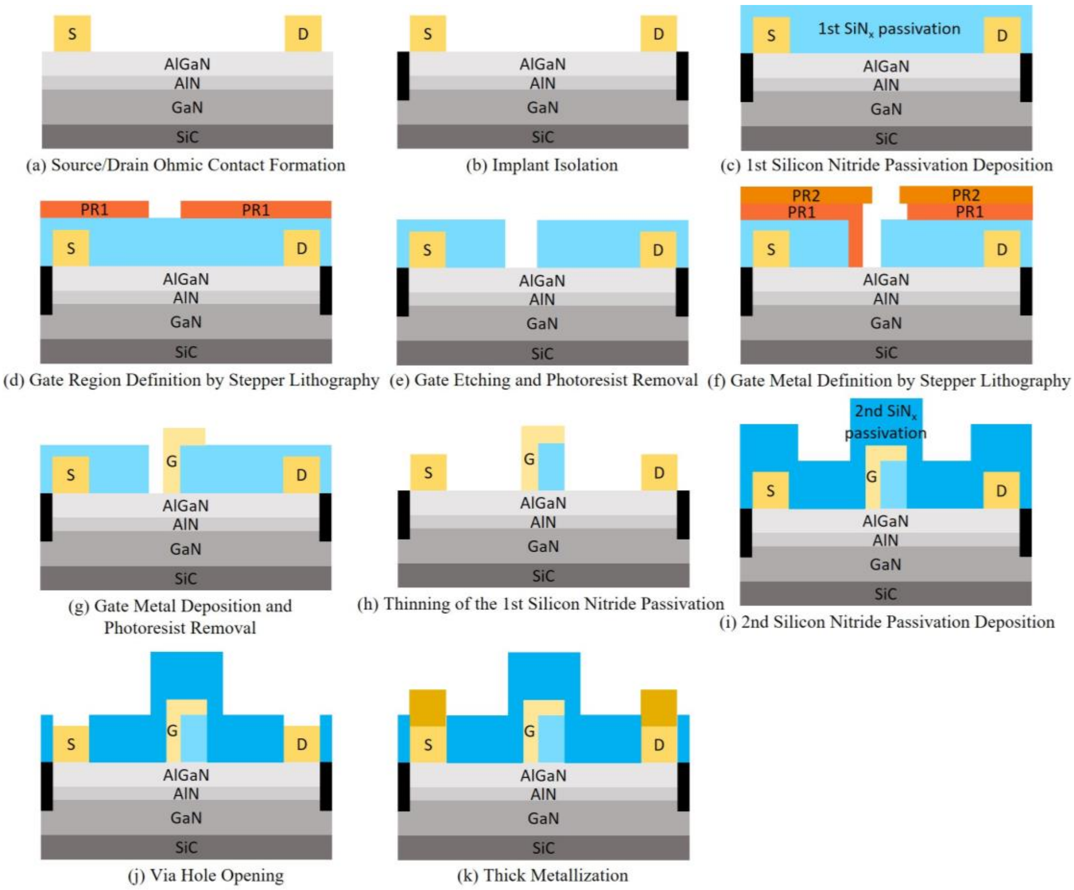

Figure 2. Process flow diagram of the AlGaN/GaN HEMT.

3. Results and Discussion

The DC characteristics of the 4 × 50 µm AlGaN/GaN HEMTs were measured using Keysight B1505A. Figure 3 shows the typical I_{DS}-V_{GS} and G_m-V_{GS} characteristics at V_{DS} = 20 V for 4 × 50 µm AlGaN/GaN HEMT devices with different SiN_x thicknesses (150 nm, 200 nm, and 250 nm). While the SiN_x thickness increases from 150 nm to 200 nm, the device exhibits an increase in the saturation drain current (I_{DSS}) from 766.5 mA/mm to 861 mA/mm, and the maximum transconductance ($G_{m,max}$) increases from 290.1 mS/mm to 312.9 mS/mm. Increasing the SiN_x thickness to 250 nm no longer significantly increases the I_{DSS} and $G_{m,max}$ of the device, as shown in Table 1. Compared to other thicknesses, the device with a SiN_x thickness of 250 nm exhibits the highest I_{DSS} and $G_{m,max}$. The increase in the device's current and G_m is due to the increase in the thickness of the SiN_x passivation layer, which leads to an increase in the biaxial tensile stress applied to the AlGaN layer, further increasing the surface charge density at the heterointerface [34,35]. Furthermore, the threshold voltage (V_{th}) for a 150 nm SiN_x thickness is −3.1 V, whereas the V_{th} for SiN_x thicknesses of both 200 nm and 250 nm is −3.7 V. The V_{th} is defined as the V_{GS} when I_{DS} = 1 mA/mm.

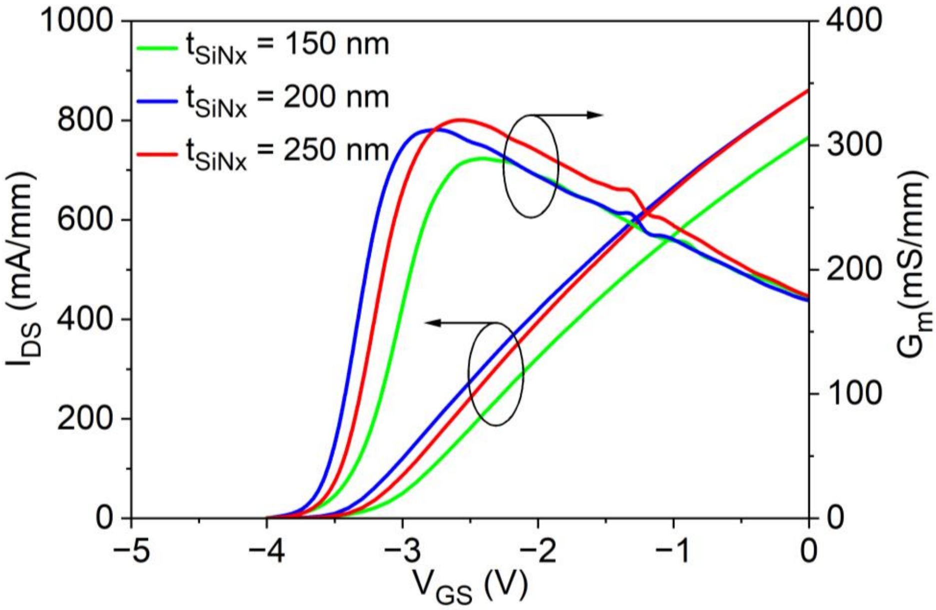

Figure 3. I_{DS}-V_{GS} characteristics and G_m of the AlGaN/GaN HEMT with various SiN_x thicknesses at V_{DS} = 20 V.

Table 1. DC characteristics of the devices with various SiN_x thicknesses at V_{DS} = 20 V.

Parameters	t_{SiNx}		
	150 nm	**200 nm**	**250 nm**
I_{DSS} (mA/mm)	766.5	861	861.5
$G_{m,max}$ (mS/mm)	290.1	312.9	320.9
V_{th} (V)	−3.1	−3.7	−3.7
GVS (V)	1.0	1.1	1.2
a_1	−0.52938	−0.47639	−0.51950
a_3	−0.25548	−0.22635	−0.24283
a_3/a_1	0.48260	0.47514	0.46743
a_5	−0.00589	−0.00491	−0.00528
a_5/a_1	0.01113	0.01031	0.01016

To further analyze the linearity, a polynomial curve fitting technique is applied to the transfer characteristic function of these devices, as shown in Equation (1) [36].

$$I_{DS}(V_{GS}) = a_0 + a_1 V_{GS} + a_2 V_{GS}^2 + a_3 V_{GS}^3 + a_4 V_{GS}^4 + a_5 V_{GS}^5 \quad (1)$$

In addition, Equation (2) can be used to estimate the IM3 levels generated by the device [37]. Equation (3) illustrates the relationship between OIP3, transconductance (G_m), drain conductance (G_{ds}), and G_m'' [38].

$$\mathrm{IM3} = \frac{3}{8} a_3 A^3 + \frac{50}{32} a_5 A^5 \quad (2)$$

$$\text{OIP3} \propto \frac{(G_m)^3}{G''_m G_{ds}^2 R_L} \quad (3)$$

The linearity of the device is primarily determined by the flatness of the G_m profile. In other words, the coefficient a_1 should be larger, whereas the ratios a_3/a_1 and a_5/a_1 should be minimized [39]. The polynomial curve fitting coefficients and the gate voltage swing (GVS), defined as a 10% drop in $G_{m,max}$, are presented in Table 1. Compared to devices with SiN_x thicknesses of 150 nm and 200 nm, the device with a SiN_x thickness of 250 nm exhibits lower a_3/a_1 and a_5/a_1 values, indicating that the device with a SiN_x thickness of 250 nm has better linearity. Furthermore, the two-tone measurement results at the end of the article also indicate an improvement in the linearity of the devices with thicker SiN_x.

Next, the S-parameters of the 4 × 50 µm devices with different SiN_x thicknesses (150, 200, and 250 nm) were measured using a Keysight E8361A PNA Network Analyzer in the frequency range from 100 MHz to 67 GHz, as shown in Figure 4. The values of f_T can be obtained by converting the measured S-parameters to H-parameters, whereas the values of f_{max} can be obtained by extrapolating the gain curve with a slope of −20 dB/decade. When increasing the SiN_x thickness from 150 nm to 250 nm, the f_T value increases from 33.7 GHz to 53.1 GHz, as indicated in Table 2. Furthermore, there is an increase in f_{max}, which improves from 76.9 GHz to 138.9 GHz. The gate stem height changes due to the varying SiN_x thicknesses. According to the definitions of f_T and f_{max} in Equations (4) and (5), increasing the SiNx thickness to enhance the device's G_m will result in higher f_T and f_{max} values [40]. Increasing the gate stem height also reduces C_{gs} and C_{gd}, further enhancing the f_T and f_{max} of the device [40]. Moreover, C_{gs} will also be affected when the gate is facing towards the drain side [41]. However, increasing the gate stem height to 300 nm does not lead to a further significant reduction in the capacitance [42]. Additionally, higher gate stem heights contribute to an increase in the gate resistance (R_g) of the device.

$$f_T = \frac{g_m/2\pi}{\left(C_{gs}+C_{gd}\right) \times [1+(R_s+R_d)g_0] + g_m C_{gd}(R_s+R_d)} \cong \frac{g_m}{2\pi\left(C_{gs}+C_{gd}\right)} \quad (4)$$

$$f_{max} = \frac{f_T}{2\sqrt{g_0\left(R_g+R_s\right)+2f_T C_{gd} R_g}} \quad (5)$$

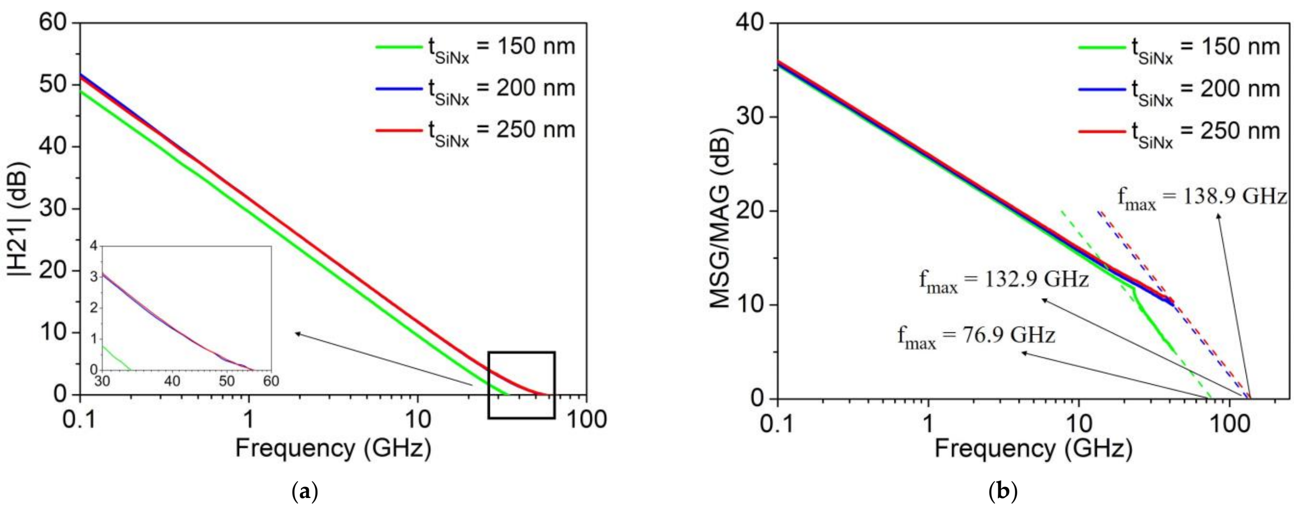

Figure 4. (**a**) ∣H21∣ and (**b**) MSG/MAG versus frequency for AlGaN/GaN HEMTs with different SiNx thicknesses.

Table 2. The f_T and f_{max} values of the devices with SiN_x thicknesses of (a) 150 nm, (b) 200 nm, and (c) 250 nm.

Parameters	t_{SiNx}		
	150 nm	**200 nm**	**250 nm**
f_T	33.7	51.9	53.1
f_{max}	76.9	132.9	138.9

Figure 5 shows the load-pull measurement results at 28 GHz for 4 × 50 μm devices with three different SiN_x thicknesses (150 nm, 200 nm, and 250 nm). All devices were measured at a bias of class AB (1/4 I_{DSS}, I_{DSS} = I_{DS} at V_{GS} = 0) and V_{DS} = 20 V. When increasing the SiN_x thickness of the device from 150 nm to 200 nm, the maximum output power density ($P_{out,max}$) increases from 2.21 W/mm to 2.61 W/mm. Furthermore, when increasing the SiN_x thickness from 200 nm to 250 nm, $P_{out,max}$ increases from 2.61 W/mm to 2.72 W/mm. From the load-pull measurement results, it can be observed that the P_{out}, PAE, and linear gain of the device show improvement when the SiN_x thickness is increased from 150 nm to 250 nm. The device with a 250 nm SiN_x thickness exhibits the best power performance, with a $P_{out,max}$ of 2.72 W/mm, PAE_{max} of 31.78%, and a linear gain of 10.68 dB. Therefore, increasing the thickness of SiN_x improves the power performance of the device.

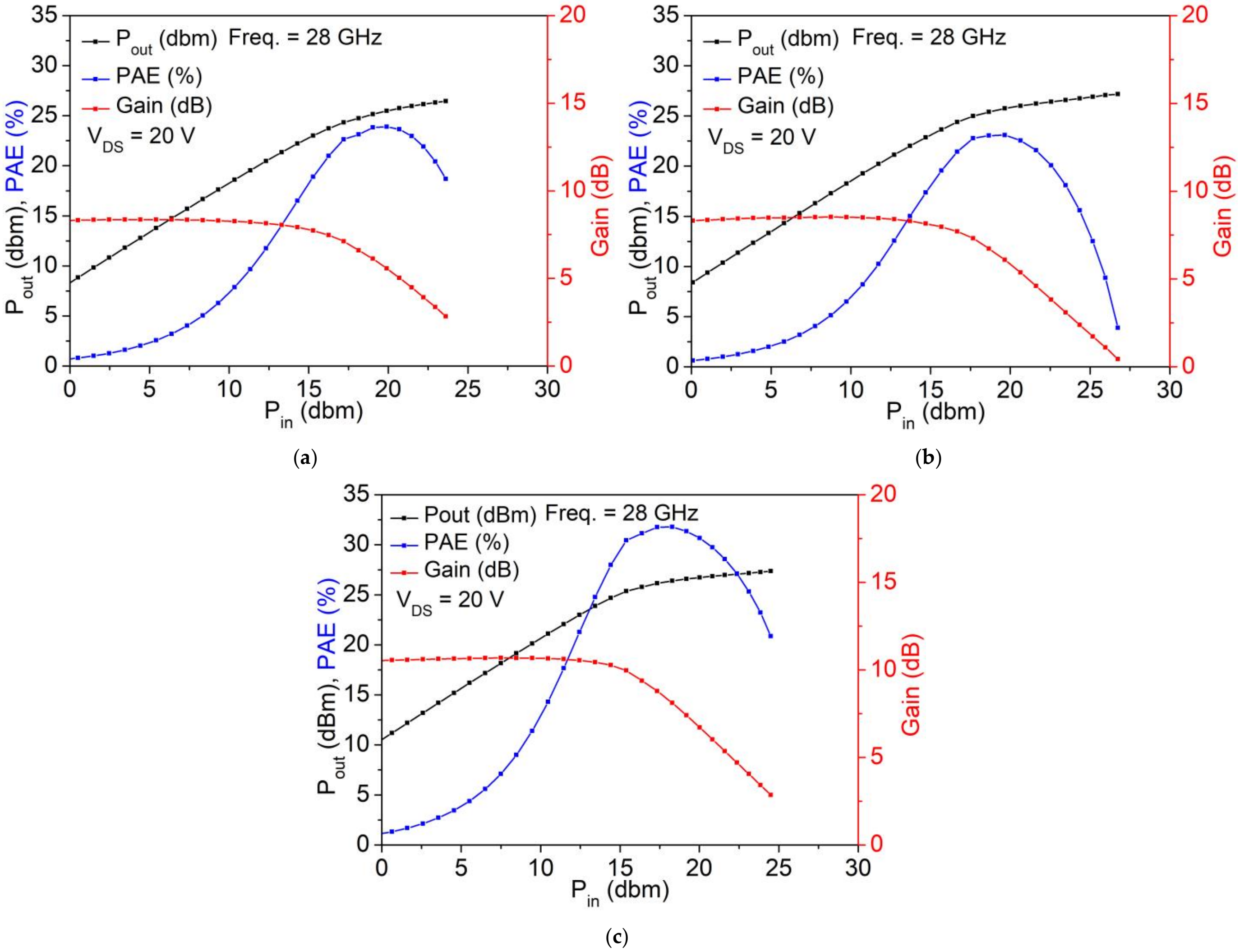

Figure 5. SiN_x thicknesses of (**a**) 150 nm, (**b**) 200 nm, and (**c**) 250 nm for the 4 × 50 μm device's power performance at 28 GHz.

To evaluate the linearity of the devices, two-tone measurements were performed at 28 GHz with a 5 MHz tone spacing using the Keysight E8267D signal generator, N9030B spectrum analyzer, U84888A power sensor, N6700C modular power system, and an AMP4072 power amplifier. Figure 6 shows the two-tone measurement results at 28 GHz for 4 × 50 μm devices with different SiN_x thicknesses. During the measurements, each device was measured at a bias of class AB (1/4 I_{DSS}, I_{DSS} = I_{DS} at V_{GS} = 0) and V_{DS} = 20 V. The measurement results show that the OIP3 value improves from 35.60 dBm to 40.87 dBm when the SiN_x thickness of the device is increased from 150 nm to 250 nm. Based on the previous polynomial curve fitting results, it can be observed that as the SiN_x thickness increases, the ratios of a_3/a_1 and a_5/a_1 decrease, resulting in an improvement in the device's linearity. Moreover, the increase in OIP3 could be attributed to the increase in SiN_x thickness, which leads to a higher current and changes in the G_m distribution, thereby enhancing the linearity of the device.

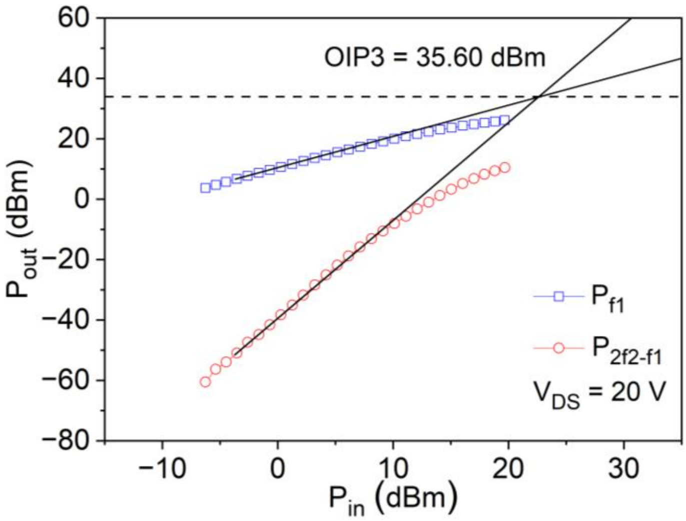

(**a**)

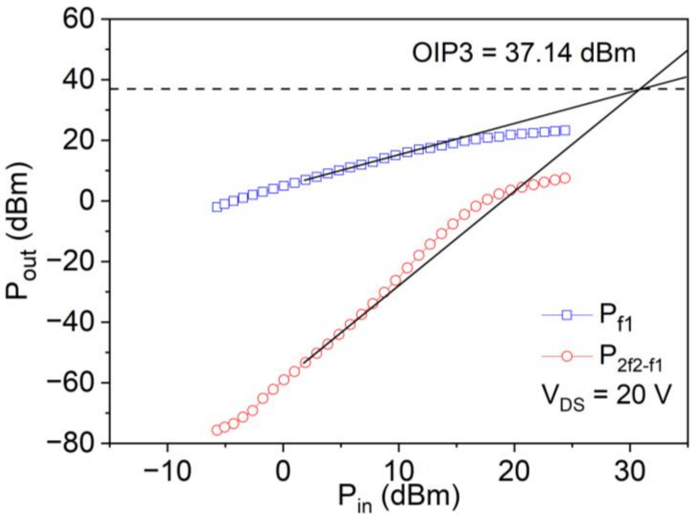

(**b**)

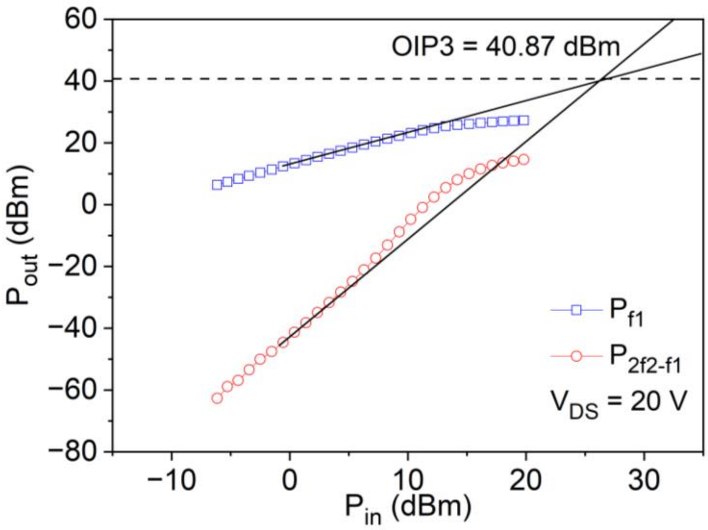

(**c**)

Figure 6. Two-tone measurement results at 28 GHz for the 4 × 50 μm devices with SiN_x thicknesses of (**a**) 150 nm, (**b**) 200 nm, and (**c**) 250 nm.

4. Conclusions

In this paper, the effects of increasing the SiN_x thickness on the characteristics of AlGaN/GaN HEMTs were investigated. The DC measurement results indicate that as the

SiN_x thickness increases, the current and G_m for the device also increase. The device's f_T and f_{max} also improve with an increase in the SiN_x thickness. For the 4 × 50 µm device with a SiN_x thickness of 250 nm, the load-pull measurement results at 28 GHz show a $P_{out,max}$ of 2.72 W/mm, a PAE_{max} of 31.78%, and a linear gain of 10.68 dB. Furthermore, the two-tone measurement results show that the improvement in OIP3 is due to the increase in the current for the device, resulting in a change in the G_m profile. The final results show that when the SiN_x thickness of the device increases from 150 nm to 200 nm, and even up to 250 nm, its characteristics such as I_{DSS}, $G_{m,max}$, $P_{out,max}$, f_T, f_{max}, and OIP3 improve. Thus, we have demonstrated that device characteristics can be improved by increasing the SiN_x thickness to a sufficient value, such as 250 nm.

Author Contributions: Conceptualization, C.-W.H. and Y.-C.L.; methodology, C.-W.H. and Y.-C.L.; validation, Y.-C.L.; investigation, C.-W.H.; resources, E.-Y.C.; data curation, C.-W.H. and Y.-C.L.; writing—original draft preparation, C.-W.H.; writing—review and editing, C.-W.H., Y.-C.L., M.-W.L., and E.-Y.C.; supervision, Y.-C.L. and E.-Y.C.; project administration, Y.-C.L. and E.-Y.C.; funding acquisition, E.-Y.C. All authors have read and agreed to the published version of the manuscript.

Funding: This study was financially supported by the "Center for the Semiconductor Technology Research" from The Featured Areas Research Center Program within the framework of the Higher Education Sprout Project by the Ministry of Education (MOE) in Taiwan. This study was also supported in part by the Ministry of Science and Technology, Taiwan, under Grant NSTC 111-2218-E-A49-021, NSTC 111-2634-F-A49-008, NSTC 111-2221-E-A49-173-MY3, and NSTC 112-2622-8-A49-013-SB.

Data Availability Statement: The data presented in this paper are available upon request from the corresponding author.

Conflicts of Interest: The authors declare no conflict of interest.

References

1. Nakajima, S. GaN HEMTs for 5G base station applications. In Proceedings of the 2018 IEEE International Electron Devices Meeting (IEDM), San Francisco, CA, USA, 1–5 December 2018; pp. 14.2.1–14.2.4.
2. Yuk, K.; Branner, G.R.; Cui, C. Future directions for GaN in 5G and satellite communications. In Proceedings of the 2017 IEEE 60th International Midwest Symposium on Circuits and Systems (MWSCAS), Boston, MA, USA, 6–9 August 2017; pp. 803–806.
3. Mishra, U.K.; Parikh, P.; Wu, Y.-F. AlGaN/GaN HEMTs-an overview of device operation and applications. *Proc. IEEE* **2002**, *90*, 1022–1031. [CrossRef]
4. Tewari, R.C.; Palo, P.; Maiti, J.; Routray, A. GaN-based Radar Micro-Doppler Augmentation for High Accuracy Fall Detection System. In Proceedings of the IECON 2022—48th Annual Conference of the IEEE Industrial Electronics Society, Brussels, Belgium, 17–20 October 2022; pp. 1–6.
5. Sun, R.; Lai, J.; Chen, W.; Zhang, B. GaN Power Integration for High Frequency and High Efficiency Power Applications: A Review. *IEEE Access* **2020**, *8*, 15529–15542. [CrossRef]
6. Palacios, T.; Chakraborty, A.; Rajan, S.; Poblenz, C.; Keller, S.; DenBaars, S.P.; Speck, J.S.; Mishra, U.K. High-power AlGaN/GaN HEMTs for Ka-band Applications. *IEEE Electron Device Lett.* **2005**, *26*, 781–783. [CrossRef]
7. Wang, Z.; Yang, D.; Cao, J.; Wang, F.; Yao, Y. A novel technology for turn-on voltage reduction of high-performance lateral heterojunction diode with source-gate shorted anode. *Superlattices Microstruct.* **2019**, *125*, 144–150. [CrossRef]
8. Wang, Z.; Zhang, Z.; Wang, S.; Chen, C.; Wang, Z.; Yao, Y. Design and Optimization on a Novel High-Performance Ultra-Thin Barrier AlGaN/GaN Power HEMT With Local Charge Compensation Trench. *Appl. Sci.* **2019**, *9*, 3054. [CrossRef]
9. Wang, F.; Chen, W.; Sun, R.; Wang, Z.; Zhou, Q.; Zhang, B. An analytical model on the gate control capability in p-GaN Gate AlGaN/GaN high-electron-mobility transistors considering buffer acceptor traps. *J. Phys. D Appl. Phys.* **2020**, *54*, 095107. [CrossRef]
10. Matsunami, H. State-of-the-art wide band-gap semiconductors for power electronic devices. In Proceedings of the International Meeting for Future of Electron Devices, Kyoto, Japan, 26–28 July 2004; pp. 21–22.
11. Flack, T.J.; Pushpakaran, B.N.; Bayne, S.B. GaN Technology for Power Electronic Applications: A Review. *J. Electron. Mater.* **2016**, *45*, 2673–2682. [CrossRef]
12. Khandelwal, S.; Goyal, N.; Fjeldly, T.A. A Physics-Based Analytical Model for 2DEG Charge Density in AlGaN/GaN HEMT devices. *IEEE Trans. Electron Devices* **2011**, *58*, 3622–3625. [CrossRef]
13. Miranda Calero, J.A.; Rituerto-Gonzalez, E.; Luis-Mingueza, C.; Canabal, M.F.; Barcenas, A.R.; Lanza-Gutierrez, J.M.; Pelaez-Moreno, C.; Lopez-Ongil, C. Bindi: Affective Internet of Things to Combat Gender-Based Violence. *IEEE Internet Things J.* **2022**, *9*, 21174–21193. [CrossRef]

14. Ropero, F.; Vaquerizo-Hdez, D.; Muñoz, P.; Barrero, D.F.; R-Moreno, M.D. LARES: An AI-based teleassistance system for emergency home monitoring. *Cogn. Syst. Res.* **2019**, *56*, 213–222. [CrossRef]
15. Darwish, A.M.; Boutros, K.; Luo, B.; Huebschman, B.D.; Viveiros, E.; Hung, H.A. AlGaN/GaN Ka-Band 5-W MMIC Amplifier. *IEEE Trans. Microw. Theory Tech.* **2006**, *54*, 4456–4463. [CrossRef]
16. Micovic, M.; Brown, D.F.; Regan, D.; Wong, J.; Tang, Y.; Herrault, F.; Santos, D.; Burnham, S.D.; Tai, J.; Prophet, E.; et al. High Frequency GaN HEMTs for RF MMIC Applications. In Proceedings of the 2016 IEEE International Electron Devices Meeting (IEDM), San Francisco, CA, USA, 3–7 December 2016; pp. 3.3.1–3.3.4.
17. Moon, J.S.; Wong, D.; Hu, M.; Hashimoto, P.; Antcliffe, M.; McGuire, C.; Micovic, M.; Willadson, P. 55% PAE and High Power Ka-Band GaN HEMTs with Linearized Transconductance via n^+ GaN Source Contact Ledge. *IEEE Electron Device Lett.* **2008**, *29*, 834–837. [CrossRef]
18. Nakatani, K.; Yamaguchi, Y.; Komatsuzaki, Y.; Sakata, S.; Shinjo, S.; Yamanaka, K. A Ka-Band High Efficiency Doherty Power Amplifier MMIC using GaN-HEMT for 5G Application. In Proceedings of the 2018 IEEE MTT-S International Microwave Workshop Series on 5G Hardware and System Technologies (IMWS-5G), Dublin, Ireland, 30–31 August 2018; pp. 1–3.
19. Nilchi, J.N.; Liu, R.; Li, S.; Akgul, M.; Rocheleau, T.O.; Nguyen, C.T.-C. Third order intermodulation distortion in capacitive-gap transduced micromechanical filters. In Proceedings of the 2015 Joint Conference of the IEEE International Frequency Control Symposium & the European Frequency and Time Forum, Denver, CO, USA, 12–16 April 2015; pp. 5–10.
20. Toole, B.; Plett, C.; Cloutier, M. RF circuit implications of moderate inversion enhanced linear region in MOSFETs. *IEEE Trans. Circuits Syst. I* **2004**, *51*, 319–328. [CrossRef]
21. Vuolevi, J.H.K.; Rahkonen, T.; Manninen, J.P.A. Measurement technique for characterizing memory effects in RF power amplifiers. *IEEE Trans. Microw. Theory Tech.* **2001**, *49*, 1383–1389. [CrossRef]
22. Chiu, H.-C.; Fu, J.S.; Chen, C.-W. RF performance of GaAs pHEMT switches with various upper/lower δ-doped ratio designs. *Solid-State Electron.* **2009**, *53*, 181–184. [CrossRef]
23. Liu, Z.H.; Ng, G.I.; Arulkumaran, S.; Maung, Y.K.; Teo, K.L.; Foo, S.C.; Sahmuganathan, V. Improved Linearity for Low-Noise Applications in 0.25-μm GaN MISHEMTs Using ALD Al_2O_3 as Gate Dielectric. *IEEE Electron Device Lett.* **2010**, *31*, 803–805. [CrossRef]
24. Guidry, M.; Romanczyk, B.; Li, H.; Ahmadi, E.; Wienecke, S.; Zheng, X.; Keller, S.; Mishra, U.K. Demonstration of 30 GHz OIP3/PDC > 10 dB by MM-wave n-polar deep recess MISHEMTs. In Proceedings of the 2019 14th European Microwave Integrated Circuits Conference (EuMIC), Paris, France, 30 September–1 October 2019; pp. 64–67.
25. Zhang, F.; Zheng, X.; Zhang, H.; Mi, M.; He, Y.; Du, M.; Ma, X.; Hao, Y. Linearity Enhancement of AlGaN/GaN HEMTS with Selective-Area Charge Implantation. *IEEE Electron Device Lett.* **2022**, *43*, 1838–1841. [CrossRef]
26. Wang, P.; Ma, X.; Mi, M.; Zhang, M.; Zhu, J.; Zhou, Y.; Wu, S.; Liu, J.; Yang, L.; Hou, B.; et al. Influence of Fin-Like Configuration Parameters on the Linearity of AlGaN/GaN HEMTs. *IEEE Trans. Electron Devices* **2021**, *68*, 1563–1569. [CrossRef]
27. Lee, M.-W.; Lin, Y.-C.; Hsu, H.-T.; Gamiz, F.; Chang, E.-Y. Improvement of AlGaN/GaN HEMTs Linearity Using Etched-Fin Gate Structure for Ka Band Applications. *Micromachines* **2023**, *14*, 931. [CrossRef] [PubMed]
28. Martinez, R.P.; Munzer, D.J.; Zhou, X.Y.; Shankar, B.; Schmidt, E.-M.; Wildnauer, K.; Wu, B.; Murmann, B.; Chowdhury, S. Best Practices to Quantify Linearity Performance of GaN HEMTs for Power Amplifier Applications. In Proceedings of the 2021 IEEE 8th Workshop on Wide Bandgap Power Devices and Applications (WiPDA), Redondo Beach, CA, USA, 7–11 November 2021; pp. 85–89.
29. Bhardwaj, N.; Upadhyay, B.B.; Parvez, B.; Pohekar, P.; Yadav, Y.; Sahu, A.; Patil, M.; Basak, S.; Sahu, J.; Sabiha, F.S.; et al. Improved RF-DC characteristics and reduced gate leakage in GaN MOS-HEMTs using thermally grown Nb_2O_5 Gate Dielectric. *Phys. Scr.* **2022**, *98*, 015805. [CrossRef]
30. Visvkarma, A.K.; Laishram, R.; Kapoor, S.; Rawal, D.S.; Vinayak, S.; Saxena, M. Improvement in DC and pulse characteristics of AlGaN/GaN HEMT by employing dual metal gate structure. *Semicond. Sci. Technol.* **2019**, *34*, 105013. [CrossRef]
31. Kwak, H.-T.; Chang, S.-B.; Kim, H.-J.; Jang, K.-W.; Yoon, H.; Lee, S.-H.; Lim, J.-W.; Kim, H.-S. Operational Improvement of AlGaN/GaN High Electron Mobility Transistor by an inner Field-Plate Structure. *Appl. Sci.* **2018**, *8*, 974. [CrossRef]
32. Rawat, A.; Surana, V.K.; Meer, M.; Bhardwaj, N.; Ganguly, S.; Saha, D. Gate Current Reduction and Improved DC/RF Characteristics in GaN-Based MOS-HEMTs Using Thermally Grown TiO_2 as a Dielectric. *IEEE Trans. Electron Devices* **2019**, *66*, 2557–2562. [CrossRef]
33. Huang, S.; Liu, X.; Wang, X.; Kang, X.; Zhang, J.; Fan, J.; Shi, J.; Wei, K.; Zheng, Y.; Gao, H.; et al. Ultrathin-Barrier AlGaN/GaN Heterostructure: A Recess-Free Technology for Manufacturing High-Performance GaN-on-Si power Devices. *IEEE Trans. Electron Devices* **2018**, *65*, 207–214. [CrossRef]
34. Mastro, M.A.; LaRoche, J.R.; Bassim, N.D.; Eddy, C.R. Simulation on the effect of non-uniform strain from the passivation layer on AlGaN/GaN HEMT. *Microelectron. J.* **2005**, *36*, 705–711. [CrossRef]
35. Jeon, C.M.; Lee, J.-L. Effects of tensile stress induced by silicon nitride passivation on electrical characteristics of AlGaN/GaN heterostructure field-effect transistors. *Appl. Phys. Lett.* **2005**, *86*, 172101. [CrossRef]
36. Lin, Y.C.; Chang, E.Y.; Yamaguchi, H.; Hirayama, Y.; Chang, X.Y.; Chang, C.Y. Device Linearity Comparison of Uniformly Doped and δ-Doped $In_{0.52}Al_{0.48}As/In_{0.6}Ga_{0.4}As$ Metamorphic HEMTs. *IEEE Electron Device Lett.* **2006**, *27*, 535–537. [CrossRef]
37. Lin, Y.-C.; Chang, E.Y.; Yamaguchi, H.; Wu, W.-C.; Chang, C.-Y. A δ-Doped InGaP/InGaAs pHEMT With Different Doping Profiles for Device-Linearity Improvement. *IEEE Trans. Electron Devices* **2007**, *54*, 1617–1625. [CrossRef]

38. Hsu, C.-H.; Shih, W.-C.; Lin, Y.-C.; Hsu, H.-T.; Hsu, H.-H.; Huang, Y.-X.; Lin, T.-W.; Wu, C.-H.; Wu, W.-H.; Maa, J.-S.; et al. Improved linearity and reliability in GaN metal–oxide–semiconductor high-electron-mobility transistors using nanolaminate La_2O_3/SiO_2 gate dielectric. *Jpn. J. Appl. Phys.* **2016**, *55*, 04EG04. [CrossRef]
39. Chiu, H.-C.; Yang, S.-C.; Chien, F.-T.; Chan, Y.-J. Improved device linearity of AlGaAs/InGaAs HFETs by a second mesa etching. *IEEE Electron Device Lett.* **2002**, *23*, 1–3. [CrossRef]
40. Lee, P.-H.; Lin, Y.-C.; Hsu, H.-T.; Tsao, Y.-F.; Dee, C.-F.; Su, P.; Chang, E.Y. A Tall Gate Stem GaN HEMT with Improved Power Density and Efficiency at Ka-band. *IEEE J. Electron Devices Soc.* **2023**, *11*, 36–42. [CrossRef]
41. Riedmuller, S.; Jacquet, J.-C.; Madel, M.; Chang, C.; Callet, G.; Piotrowicz, S.; Delage, S.; Gruenenpuett, J.; Blanck, H.; Scholz, F. A three-layer resist process for T- and Γ-gates in high electron mobility transistor fabrication. In Proceedings of the 2018 48th European Microwave Conference (EuMC), Madrid, Spain, 23–27 September 2018; pp. 1277–1280.
42. Song, B.; Berardi, S.-R.; Wang, R.; Guo, J.; Hu, Z.; Yue, Y.; Faria, F.; Schuette, M.; Ketterson, A.; Beam, E.; et al. Effect of Fringing Capacitances on the RF Performance of GaN HEMTs with T-Gates. *IEEE Trans. Electron Devices* **2014**, *61*, 747–754. [CrossRef]